

Morphologies of Wolf-Rayet Planetary Nebulae based on IFU Observations

A. Danehkar¹ ¹ Department of Astronomy, University of Michigan, Ann Arbor, MI 48109, USA; danehkar@umich.edu

Abstract: Integral field unit (IFU) spectroscopy of planetary nebulae (PNe) provides a plethora of information about their morphologies and ionization structures. An IFU survey of a sample of PNe around hydrogen-deficient stars has been conducted with the Wide Field Spectrograph (WiFeS) on the ANU 2.3-m telescope. In this paper, we present the H α kinematic observations of the PN M2-42 with a weak emission-line star (*wels*), and the compact PNe Hen 3-1333 and Hen 2-113 around Wolf-Rayet ([WR]) stars from this WiFeS survey. We see that the ring and point-symmetric knots previously identified in the velocity [N II] channels of M2-42 are also surrounded by a thin exterior ionized H α halo, whose polar expansion is apparently faster than the low-ionization knots. The velocity-resolved H α channel maps of Hen 3-1333 and Hen 2-113 also suggest that the faint multipolar lobes may get to a projected outflow velocity of $\sim 100 \pm 20 \text{ km s}^{-1}$ far from the central stars. Our recent kinematic studies of the WiFeS/IFU survey of other PNe around [WR] and *wels* mostly hint at elliptical morphologies, while collimated outflows are present in many of them. As the WiFeS does not have adequate resolution for compact ($\leq 6 \text{ arcsec}$) PNe, future high-resolution spatially-resolved observations are necessary to unveil full details of their morpho-kinematic structures.

Keywords: planetary nebulae; Wolf-Rayet stars; morphology; integral field spectroscopy

1. Introduction

Asymptotic giant branch (AGB) stars with low to intermediate initial masses (1–8 M_{\odot}) expel hydrogen-rich envelopes, which are subsequently photo-ionized by UV radiation from post-AGB degenerate cores, resulting in so-called *planetary nebulae* (PNe). The gaseous structures of these expanding ionized H-rich envelopes seen in the optical band, thanks to photoionization, are modified by stellar winds from their remnant central stars as they move on their evolutionary path toward the white dwarf stage. Their strong collisionally excited line emissions reveal their morphological features to us across the Galaxy, making them powerful kinematic probes. Aside from their morphologies, PNe also shed light on mass-loss processes occurring during the AGB phase and their transition to PN (see e.g. [1–3]), as well as chemical elements produced by nucleosynthesis processes in the AGB stage (e.g. [4–6]).

A major challenge to theories in nebular astrophysics is the fact that many of them possess aspherical morphologies (see review by Balick and Frank [7]). Although single stars can generate aspherical shells, as predicted by the interacting stellar wind (ISW) theory [8] and its generalization [9], they cannot produce the highly complex elliptical and bipolar morphologies seen in recent high-resolution observations of many PNe (see e.g. [10]). It has also been proposed that binarity [11–13] and magnetic fields combined with stellar winds from a rotating single star [14,15] could also lead to aspherical morphologies. However, a single AGB star with realistic rotating speeds failed to generate a highly bipolar shell in magnetohydrodynamic simulations [16]. According to observations [17–20] and hydrodynamic simulations [21–23], the majority of aspherical morphologies appear to have formed via a binary channel.

A number of integral field unit (IFU) spectrographs on modest telescopes, such as the Wide Field Spectrograph (WiFeS [24,25]) on the Australian National University (ANU) 2.3-m telescope have made it possible to constrain the kinematic and ionization properties of several PNe [26–32]. Moreover, the Multi Unit Spectroscopic Explorer (MUSE) and the Visible Multi-Object Spectrograph (VIMOS) on the European Southern Observatory's



Citation: Danehkar, A. Morphologies of WR PNe based on IFU. *Preprints* 2022, 1, 0. <https://doi.org/>

Publisher's Note: MDPI stays neutral with regard to jurisdictional claims in published maps and institutional affiliations.



Copyright: © 2022 by the authors. Licensee MDPI, Basel, Switzerland. This article is an open access article distributed under the terms and conditions of the Creative Commons Attribution (CC BY) license (<https://creativecommons.org/licenses/by/4.0/>).

(ESO) Very Large Telescope (VLT) have recently enabled the constraint of the ionization structures of some PNe [33–36]. IFU spectroscopy allows us to spatially resolve the physical and kinematic properties of PNe, which is an important step toward understanding their morphological features in different ionization stratification layers.

An IFU survey of a sample of PNe around Wolf-Rayet ([WR]) central stars and weak emission-line stars (*wels*) were carried out with the ANU/WiFeS in April 2010 (Program No. 1100147; PI: Q.A. Parker). In particular, hydrogen-deficient [WR] stars constitute a substantial proportion ($\sim 25\%$) of central stars of PNe, which demonstrate fast expanding atmospheres and high mass-loss rates [37], as well as helium-burning products (He, C, O and Ne) on their stellar surfaces [4]. The WiFeS survey with a field-of-view of $25 \times 38 \text{ arcsec}^2$ and a spatial resolution of $1''$ provides a wealth of information about their kinematic features [26–30], as well as their physical and chemical properties [38,39]. The WiFeS offers a seeing of $\sim 2''$ and a velocity resolution of $\sim 21 \text{ km s}^{-1}$ in the red channel at $R \sim 7000$. This sample includes PNe around [WR] stars ranging from [WO 1] to [WC 6], and from [WC 9] to [WC 11] [37,40], as well as *wels* [41,42] (see Table 1 in Danehkar [29]), which could help us understand better the formation of aspherical morphologies and the mechanism scraping off hydrogen-rich layers in hydrogen-deficient degenerate cores. However, IFU spectroscopy and photoionization modeling of 4 PNe with supposed *wels* suggested that the *wels* classification could be spurious, since some assumed stellar emission lines could be of nebular origin, so three of them were then classified as hydrogen-rich O(H)-type [43]. In present study, we provide the WiFeS $H\alpha$ kinematic results of the PN M 2-42 with a *wels* (§ 2), the PNe Hen 3-1333 and Hen 2-113 with [WC 10] stars (§ 3), followed by a discussion about our recent morpho-kinematic analyses of PNe around [WR] stars and a few *wels* conducted using the WiFeS survey [29] in Section 4, and a conclusion in Section 5.

2. M 2-42: $H\alpha$ velocity channels

The PN M 2-42 (= PNG008.2–04.8) is associated with a *wels* [41]. This object, which has a relatively high density ($3 \times 10^3 \text{ cm}^{-3}$) and chemical abundances of a bit above the solar composition [39,44], could be in the Galactic bulge according to $D = 9.44 \text{ kpc}$ [45], as well as $7.4 \pm 0.6 \text{ kpc}$ derived from the surface brightness-radius correlation [46]. It contains two bipolar outflows extending from a dense central ring as revealed by long-slit [47] and IFU observations [28]. A three-dimensional (3D) morpho-kinematic model of this object was built based on the [N II] velocity-resolved channels [28], which apart from asymmetric outflows is roughly similar to the symmetric outflow model adopted by Akraś and López [47]. The IFU observations disclosed highly asymmetric features of bipolar outflows, which could be created because of the nebular interaction with the interstellar medium (ISM).

Figure 1 shows a sequence of 10 velocity-resolved continuum-subtracted $H\alpha$ flux maps of M 2-42 on a logarithmic scale collected with channel intervals of around 21 km s^{-1} . The central velocity of each channel is given at the top of the panel with respect to the LSR (local standard of rest) systemic velocity ($v_{\text{sys}} = 123 \text{ km s}^{-1}$) listed at the right-bottom corner of the whole panels. The systemic velocity was transfer to the LSR frame using the IRAF function *rvcorrect*. The gray contours in each panel show the boundary at 10 percent of the mean $H\alpha$ surface brightness based on the $H\alpha$ plate retrieved from the SuperCOSMOS H-alpha Sky Survey (SHS) [48].

A dense central ring along with a pair of detached bipolar outflows were identified by Danehkar *et al.* [28] in the [N II] $\lambda 6584$ channel maps. Additionally, the $H\alpha$ $\lambda 6563$ velocity channels show that these structures are enveloped by a faint $H\alpha$ halo, which makes it difficult to observe the separation between the detached knots and central ring as seen in low-excitation [N II] maps. The $H\alpha$ flux maps are rather similar to what we see in the SHS $H\alpha$ image (see Figure 1 in Danehkar *et al.* [28]). We should note that the $H\alpha$ IFU maps were saturated over two bright points on the main shell area (as previously pointed out by Danehkar *et al.* [28]). However, the $H\alpha$ flux channels can help us identify the faint halo

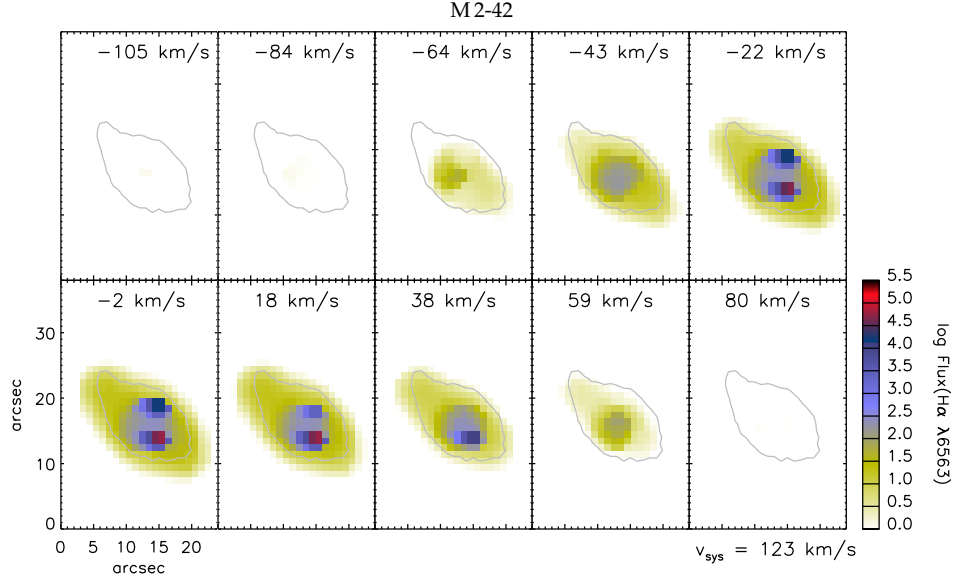


Figure 1. Velocity-resolved flux channels of M2-42 along $H\alpha$ $\lambda 6563$ at $\sim 21 \text{ km s}^{-1}$ intervals with channel velocities specified at the top in km s^{-1} . The systemic velocity (v_{sys}) in the LSR frame is given in the right bottom corner in km s^{-1} unit. The logarithmic color bar is in $10^{-15} \text{ erg s}^{-1} \text{ cm}^{-2} \text{ spaxel}^{-1}$ unit. The gray contour depicts the boundary of 10 percent of the mean $H\alpha$ surface brightness of this object in the SHS. The channels are oriented with north up and east toward the left side. Two bright points over the central shell in the flux maps are associated with $H\alpha$ emission saturation.

surrounding the bipolar outflows and the ring. Similarly, the PNe NGC 6567, NGC 6578, NGC 6629, and Sa 3-107 around *wels* were also found to contain large faint halos in the $H\alpha$ emission, which are not visible in the $[\text{N II}]$ maps [29].

The knots have a projected velocity of $\sim 15 \text{ km s}^{-1}$ respect to the central star in the $[\text{N II}]$ emission [47], which corresponds to an outflow velocity of $\sim 110 \text{ km s}^{-1}$ at the inclination of 82° adopted by Danekhar *et al.* [28]. However, the halos around the knots seem to expand with higher polar velocities in the $H\alpha$ emission. The higher outflow velocities seen in the $H\alpha$ channels could mostly be associated with the tenuous halos around the two detached N^+ low-ionization point-symmetric knots escaping from the core with slower outflow velocities. This could be a sign of the deceleration of the knots because of the interaction with the ambient medium. Similarly, the point-symmetric knots in Hb 4 were found to be decelerated by the PN-ISM interaction [29,49].

3. Hen 3-1333 and Hen 2-113: $H\alpha$ velocity channels and PV diagrams

The PNe Hen 3-1333 (= PNG332.9−09.9) and Hen 2-113 (= PNG321.0+03.9) are around late-type [WC 10] cool stars, according to the classification scheme of [40], with effective temperatures of 25 kK and 29 kK [50], respectively. These objects have extremely high densities of 10^5 cm^{-3} [39], which are typical of very young compact PNe. They also depict distinct oxygen- and carbon-rich dust characteristics of the early PN phase just after the AGB phase [51,52]. Their morphological features have been studied using the spatially-resolved $H\alpha$ maps [27], which disclosed their main orientations on the sky plane, in agreement with the *Hubble Space Telescope* (HST) imaging analyses [53,54].

In Figure 2, we present the 15 flux channel maps of Hen 3-1333 and Hen 2-113 along the $H\alpha$ emission on a logarithmic scale recorded at $\sim 21 \text{ km s}^{-1}$ velocity intervals. The channel velocity is with respect to the systemic velocity in the LSR frame provided at the right bottom corner. The continuum of each object was identified and removed from each flux channel map. Similar to Figure 1, the contours again correspond to their SHS $H\alpha$ distribution, which might illustrate the nebular borders. However, the SHS maps of

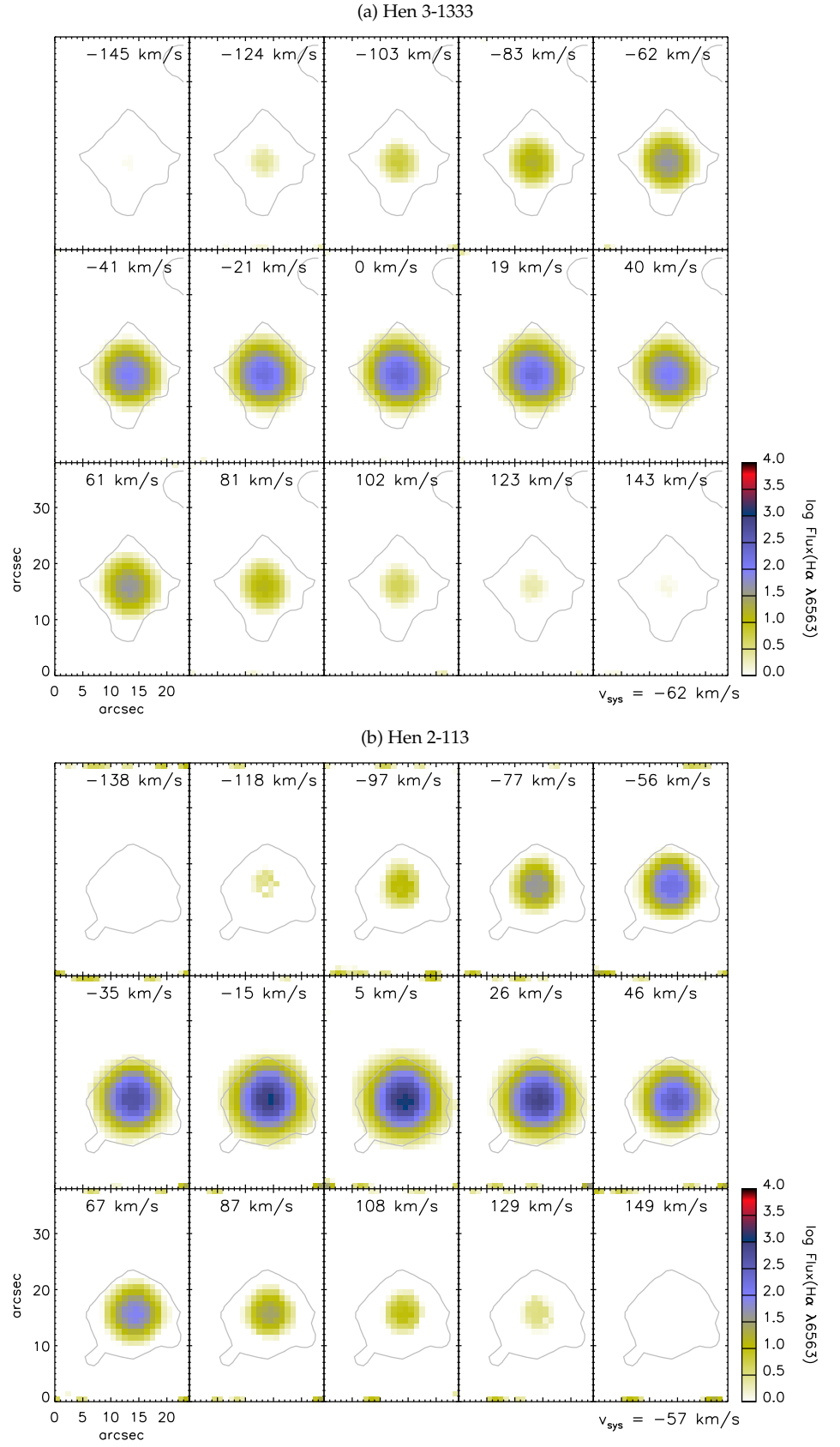


Figure 2. The same as Figure 1, but for (a) Hen 3-1333 and (b) Hen 2-113.

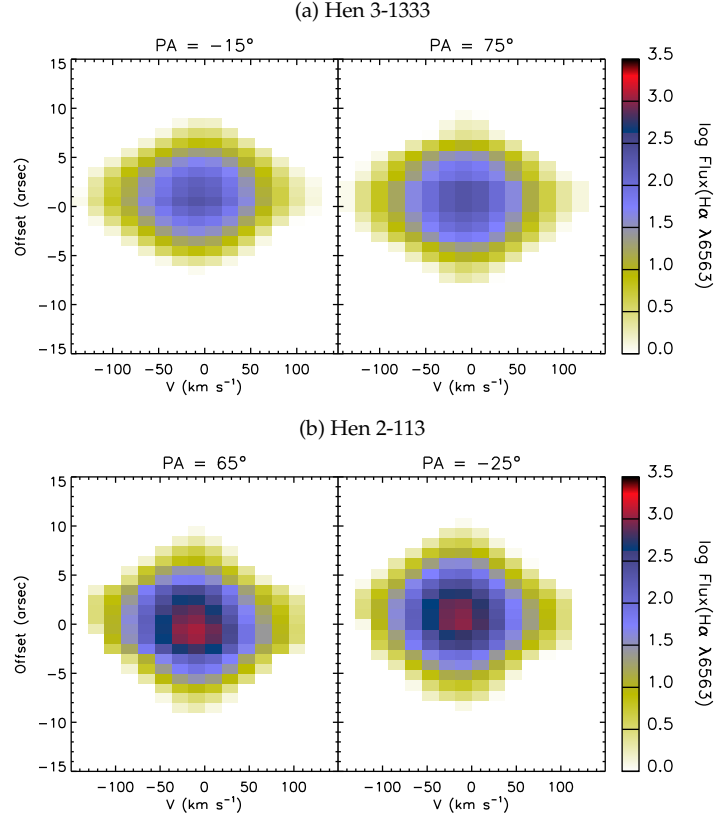


Figure 3. PV arrays of (a) Hen 3-1333 and (b) Hen 2-113 observed in the $H\alpha$ $\lambda 6563$ emission. Slits are aligned with the PA parallel to and vertical to the model's symmetric axis. The velocity in each P-V array is relative to the object's systemic velocity in km s^{-1} units. The central star is positioned at the angular offset of $0''$. The logarithmic color bar is in $10^{-15} \text{ erg s}^{-1} \text{ cm}^{-2} \text{ spaxel}^{-1}$ unit.

these two objects are largely contaminated by the point spread function (PSF) of their central stars, resulting in the PSF spikes and artifacts around the PNe. It can be seen that the tenuous multipolar lobes extending from the central bodies in Hen 3-1333 and Hen 2-113 may reach a projected expansion velocity of about $\sim 100 \pm 20 \text{ km s}^{-1}$ relative to their central stars. Previously, they found no evidence of Balmer line emission of stellar origin in these objects [50,55], so the $H\alpha$ emission profiles could be attributed to nebular ionization structures. Nevertheless, the broad $H\alpha$ wings in young, compact PNe may also be created by Rayleigh-Raman scattering [56]. We should note that the mass-weighted expansion velocities estimated from the half width at half maximum (HWHM) of the $H\alpha$ emission in the integrated spectra were found to be 32 km s^{-1} (Hen 3-1333) and 23 km s^{-1} (Hen 2-113) [27], which are mostly associated with the bright central regions. However, the velocity channel maps indicate that the outflow velocities of the faint multipolar lobes may be much higher than the mass-weighted HWHM expansion velocities. Moreover, the spatially-resolved velocity maps previously built with a single Gaussian fitting only revealed the primary orientations of the bright nebulae [27], without any details about faint outflows.

Figure 3 depicts the position-velocity (PV) arrays of Hen 3-1333 (top panels) and Hen 2-113 (bottom panels) observed in the $H\alpha$ $\lambda 6563$ emission, which were generated with two slits with different orientations: one parallel with (left panel), and another one perpendicular to the symmetric axes of the primary orientations (right panel). The main on-sky orientations of the PN Hen 3-1333 and Hen 2-113 determined by Danehkar and Parker [27] have position angles (PA) of -15° and 65° , respectively, which are adopted for the slit directions. The slits of each object were positioned on the central star. The continua in the PV

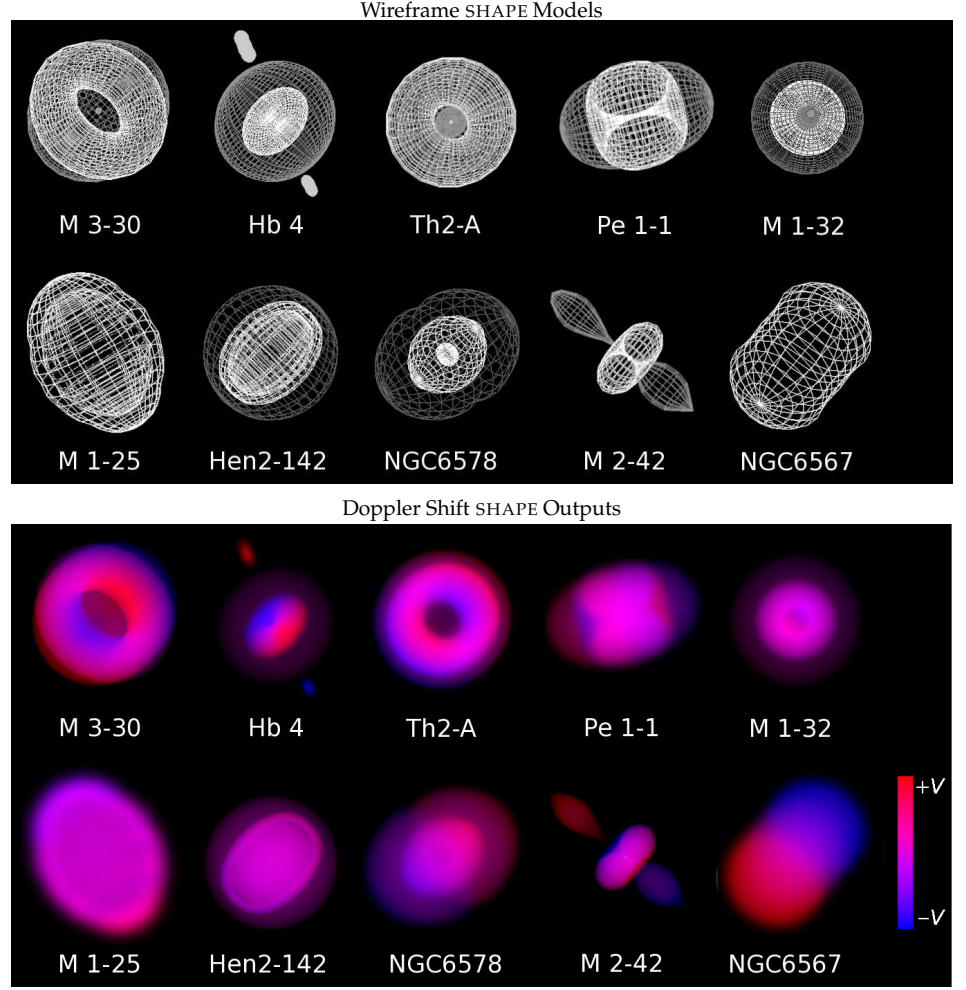


Figure 4. Wireframe SHAPE models (top panel) and their Doppler shift outputs (bottom panel) of M 3-30, Hb 4, Pe 1-1, M 1-32, M 1-25, Hen 2-142, MGC 6578, and NGC 6567 from Danehkar [29], along with Th2-A [26] and M2-42 [28]. Red and blue colors in the Doppler shift outputs are associated with redshift ($+V$) and blueshift ($-V$) effects relative to the centers, respectively. 3D interactive SHAPE models are provided by Danehkar [29] and hosted on Sketchfab (<https://skfb.ly/opFZv>).

arrays were also detected and subtracted in a way similar to the continuum-subtraction performed in the velocity channel maps. The position and velocity axes are with respect to the central star's location and the object's systemic velocity, respectively. As can be seen, the faint outflows extending from the central nebulae may get as far as projected velocities of $\sim 100 \text{ km s}^{-1}$ similar to the channel maps shown in Figure 2, while they are also extended to a radial distance of $\sim 4''$ from the central stars. Moreover, the tenuous lobes might be extended to $\sim 8''$, where the nebula emission is extremely weak for detection. Asymmetric patterns seen in the horizontal slits in both of them, but rather symmetric patterns in the vertical slits, also indicate that the faint outflows have inclinations relative to the line of sight. The inclination angles of $i = -30^\circ$ and 40° were also suggested for Hen 3-1333 and Hen 2-113 [27]. Detection of substructures of these compact objects require spatial and velocity resolution higher than the WiFeS.

4. Discussion: Morpho-kinematics of [WR] PNe

A sample of PNe surrounding hydrogen-deficient [WR] stars, including the early-type group ranging from [WO 1] to [WC 6], and the late-type group from [WC 9] to [WC 11] [37,40], as well as a few *wels* [41,42], have been studied by Danehkar [29], which might pro-

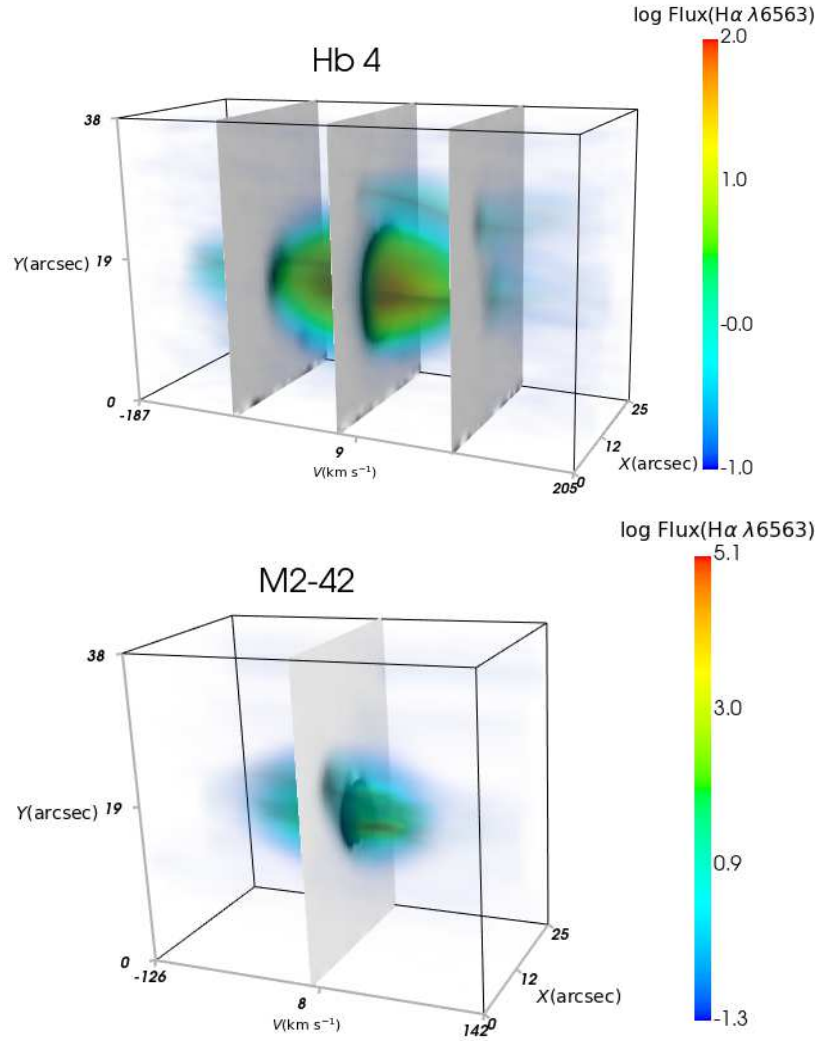


Figure 5. PPV cubes of Hb 4 (top panel) and M2-42 (bottom panel) with 3 slices at -104 , 0 , and $+102$ km s^{-1} for Hb 4, and a slice at -2 km s^{-1} for M2-42. Velocity slices of Hb 4 and M2-42 are presented in Danehkar [29] and Figure 1, respectively.

vide some clues about aspherical morphologies and hydrogen-deficient central stars. The projected velocity maps, PV diagrams, velocity channel maps, and archival images have been used to constrain their 3D geometrical models in the SHAPE program [57,58].

Figure 4 presents their wireframe SHAPE models (top panel) together with their corresponding Doppler shift maps generated by SHAPE (bottom panel). Redshift and blueshift effects with respect to the nebula center are rendered by red and blue colors, which can be compared to the two-dimensional (2D) projected radial velocity IFU maps (see Figure 1 in Danehkar [29]). Particularly, PV arrays and velocity channels created by SHAPE put constraints on the geometry with specified density and velocity laws, whereas Doppler shift rendered images (Figure 4 bottom) help us have a first-order approximation of the morphology. The final 3D models, which were built with PV diagrams and velocity-resolved channels, are presented in an interactive figure in Danehkar [29], together with the 3D object files on the Sketchfab platform (<https://skfb.ly/opFZv>).

As it can be seen, these PNe mostly have aspherical, elliptical morphologies. Moreover, collimated bipolar outflows can be easily distinguished in the position-position-velocity (PPV) cubes of Hb 4 and M2-42 as shown in Figure 5 (see [29] for velocity slices of Hb 4, and Figure 1 for M2-42). Collimated outflows expanding from the ring-shaped main

structures were also detected in the observed PV arrays of M1-32, M3-15, M3-30 [29], and Th2-A [26]. We should also mention prolate spheroid shells in NGC 6567, NGC 6578, NGC 6629, and Hen 2-142, and M1-25. Additionally, as pointed out by Danehkar [29], the IFU projected dispersion maps of Pe 1-1 hint at possible collisions between the bipolar outflow and the previous expelled materials. The kinematic ionization structure of M2-42 was previously determined from the [N II] spatially-resolved IFU maps [28], which are now complemented by the velocity-resolved H α flux maps in Sec. 2. Hen 3-1333 and Hen 2-113 around [WC 10], whose velocity channels and PV arrays are presented in Sec. 3, were also studied in detail by Danehkar and Parker [27] using the 2D projected velocity IFU maps and high-resolution *HST* images that pointed to multipolar outflows and tenuous lobes extending from their central, dense ($\sim 10^5 \text{ cm}^{-3}$ [39]) bodies.

5. Conclusion

IFU observations with cost-effective spectrographs on modest telescopes such as the ANU/WiFeS can disclose detailed morpho-kinematic properties of extended Galactic PNe (e.g. M2-42 in § 2), while they are also promising for compact (≤ 6 arcsec) PNe (e.g. Hen 3-1333 and Hen 2-113 in § 3). There are various kinematic information that can be extracted from an IFU datacube (see e.g. Figure 5), namely spatially-resolved projected velocity maps, velocity-resolved flux channels, and PV diagrams.

The H α channel maps of M2-42 in § 2 indicate that the previously identified ring and point-symmetric knots [28,47] are also covered by a low-density exterior H $^+$ halo, which cannot easily be identified with low-excitation N $^+$ mapping. The polar regions in the exterior H $^+$ halo expand (see Figure 1) apparently higher than those in the point-symmetric knots ($\sim 110 \text{ km s}^{-1}$). As point-symmetric knots are typically expected to move faster than their surrounding halos, their slowness could be an indication of the deceleration due to a collision with the surrounding medium (see also Hb 4 in [29,49]).

The velocity channels and PV diagrams of Hen 3-1333 and Hen 2-113 in § 3 also revealed that the faint outflows may approach a projected outflow velocity of $\sim 100 \pm 20 \text{ km s}^{-1}$ at $4''$ far from the central stars. However, we caution that the broad H α wings of these compact PNe may be associated with Rayleigh-Raman scattering [56]. Asymmetric PV patterns seen in the horizontal slits could also be related to moderate line-of-sight inclinations ($i = -30^\circ$ and 40°) in Hen 3-1333 and Hen 2-113. Detailed morpho-kinematic modeling of these compact PNe can be performed when kinematic observations with higher spatial and wavelength resolution are available.

The on-sky orientation of an extended symmetric nebula can easily be determined from a spatially-resolved 2D radial velocity IFU map (see Figure 1 in [29]) by comparison with a Doppler shift synthetic image created by SHAPE (Figure 4, bottom), but without full details of substructures. 3D morpho-kinematic modeling implemented using velocity-resolved channel maps and position-velocity diagrams may disentangle different structural components of an ionized nebula, which cannot be unveiled by 2D radial velocity IFU mapping.

Author Contributions: The author confirms being the sole contributor of this work and approved it for publication.

Funding: This research was partially supported by a Macquarie Research Excellence Scholarship (MQRES: 2010–2013) and a Sigma Xi Grants-in-Aid of Research (GIAR; 2013).

Data Availability Statement: The supporting data for § 4 are provided as supplementary materials in Danehkar [29], and the 3D models are available on Sketchfab (<https://skfb.ly/opFZv>). The data underlying Sections 2 and 3 will be shared on reasonable request to the author.

Acknowledgments: The author thanks the APN8 2021e organizers for providing an opportunity to present this work, Quentin Parker and David Frew for supporting the WiFeS observing run in 2010, Milorad Stupar for instructions on the WiFeS data reduction, and Kyle DePew for undertaking the 2010 WiFeS observation.

Conflicts of Interest: The authors declare no conflict of interest.

Abbreviations

The following abbreviations are used in this manuscript:

ANU	Australian National University
HST	Hubble Space Telescope
HWHM	Half Width at Half Maximum
IFU	Integral Field Unit
ISM	Interstellar Medium
LSR	Local Standard of Rest
PA	Position Angle
PN	Planetary Nebula
PSF	Point Spread Function
PPV	Position-Position-Velocity
PV	Position-Velocity
SHS	SuperCOSMOS H-alpha Sky Survey
<i>wels</i>	weak emission-line star
WiFeS	Wide Field Spectrograph
WR	Wolf-Rayet

References

- Balick, B. The evolution of planetary nebulae. I - Structures, ionizations, and morphological sequences. *AJ* **1987**, *94*, 671–678. doi:10.1086/114504.
- Schönberner, D.; Jacob, R.; Steffen, M. The evolution of planetary nebulae. III. Internal kinematics and expansion parallaxes. *A&A* **2005b**, *441*, 573–588. doi:10.1051/0004-6361:20053108.
- Kwok, S. Morphological Structures of Planetary Nebulae. *PASA* **2010**, *27*, 174–179, [[arXiv:astro-ph/0911.5571](#)]. doi:10.1071/AS09027.
- Werner, K.; Herwig, F. The Elemental Abundances in Bare Planetary Nebula Central Stars and the Shell Burning in AGB Stars. *PASP* **2006**, *118*, 183–204, [[arXiv:astro-ph/0512320](#)]. doi:10.1086/500443.
- Karakas, A.; Lattanzio, J.C. Stellar Models and Yields of Asymptotic Giant Branch Stars. *PASA* **2007**, *24*, 103–117, [[0708.4385](#)]. doi:10.1071/AS07021.
- Karakas, A.I.; van Raai, M.A.; Lugaro, M.; Sterling, N.C.; Dinerstein, H.L. Nucleosynthesis Predictions for Intermediate-Mass Asymptotic Giant Branch Stars: Comparison to Observations of Type I Planetary Nebulae. *ApJ* **2009**, *690*, 1130–1144, [[0809.1456](#)]. doi:10.1088/0004-637X/690/2/1130.
- Balick, B.; Frank, A. Shapes and Shaping of Planetary Nebulae. *ARA&A* **2002**, *40*, 439–486. doi:10.1146/annurev.astro.40.060401.093849.
- Kwok, S.; Purton, C.R.; Fitzgerald, P.M. On the origin of planetary nebulae. *ApJ* **1978**, *219*, L125–L127. doi:10.1086/182621.
- Kahn, F.D.; West, K.A. Shapes of planetary nebulae. *MNRAS* **1985**, *212*, 837–850.
- Sahai, R.; Morris, M.R.; Villar, G.G. Young Planetary Nebulae: Hubble Space Telescope Imaging and a New Morphological Classification System. *AJ* **2011**, *141*, 134, [[arXiv:astro-ph.GA/1101.2214](#)]. doi:10.1088/0004-6256/141/4/134.
- Soker, N. Why Magnetic Fields Cannot Be the Main Agent Shaping Planetary Nebulae. *PASP* **2006**, *118*, 260–269, [[arXiv:astro-ph/0501647](#)]. doi:10.1086/498829.
- Nordhaus, J.; Blackman, E.G. Low-mass binary-induced outflows from asymptotic giant branch stars. *MNRAS* **2006**, *370*, 2004–2012, [[arXiv:astro-ph/0604445](#)]. doi:10.1111/j.1365-2966.2006.10625.x.
- Nordhaus, J.; Blackman, E.G.; Frank, A. Isolated versus common envelope dynamos in planetary nebula progenitors. *MNRAS* **2007**, *376*, 599–608, [[arXiv:astro-ph/0609726](#)]. doi:10.1111/j.1365-2966.2007.11417.x.
- García-Segura, G.; Langer, N.; Różyczka, M.; Franco, J. Shaping Bipolar and Elliptical Planetary Nebulae: Effects of Stellar Rotation, Photoionization Heating, and Magnetic Fields. *ApJ* **1999**, *517*, 767–781. doi:10.1086/307205.
- García-Segura, G.; López, J.A. Three-dimensional Magnetohydrodynamic Modeling of Planetary Nebulae. II. The Formation of Bipolar and Elliptical Nebulae with Point-symmetric Structures and Collimated Outflows. *ApJ* **2000**, *544*, 336–346, [[arXiv:astro-ph/0007189](#)]. doi:10.1086/317186.
- García-Segura, G.; Villaver, E.; Langer, N.; Yoon, S.C.; Manchado, A. Single Rotating Stars and the Formation of Bipolar Planetary Nebula. *ApJ* **2014**, *783*, 74, [[arXiv:astro-ph.SR/1401.4414](#)]. doi:10.1088/0004-637X/783/2/74.
- Miszalski, B.; Acker, A.; Moffat, A.F.J.; Parker, Q.A.; Udalski, A. Binary planetary nebulae nuclei towards the Galactic bulge. I. Sample discovery, period distribution, and binary fraction. *A&A* **2009**, *496*, 813–825, [[arXiv:astro-ph.SR/0901.4419](#)]. doi:10.1051/0004-6361/200811380.

18. Jones, D.; Mitchell, D.L.; Lloyd, M.; Pollacco, D.; O'Brien, T.J.; Meaburn, J.; Vaytet, N.M.H. The morphology and kinematics of the Fine Ring Nebula, planetary nebula Sp 1, and the shaping influence of its binary central star. *MNRAS* **2012**, *420*, 2271–2279, [arXiv:astro-ph.SR/1111.2860]. doi:10.1111/j.1365-2966.2011.20192.x.
19. Tyndall, A.A.; Jones, D.; Lloyd, M.; O'Brien, T.J.; Pollacco, D. A study of the kinematics and binary-induced shaping of the planetary nebula HaTr 4. *MNRAS* **2012**, *422*, 1804–1811, [arXiv:astro-ph.SR/1202.3124]. doi:10.1111/j.1365-2966.2012.20755.x.
20. Huckvale, L.; Prouse, B.; Jones, D.; Lloyd, M.; Pollacco, D.; López, J.A.; O'Brien, T.J.; Sabin, L.; Vaytet, N.M.H. Spatio-kinematic modelling of Abell 65, a double-shelled planetary nebula with a binary central star. *MNRAS* **2013**, *434*, 1505–1512, [arXiv:astro-ph.SR/1306.4272]. doi:10.1093/mnras/stt1109.
21. Chen, Z.; Nordhaus, J.; Frank, A.; Blackman, E.G.; Balick, B. Three-dimensional hydrodynamic simulations of L₂ Puppis. *MNRAS* **2016**, *460*, 4182–4187, [arXiv:astro-ph.SR/1602.06142]. doi:10.1093/mnras/stw1305.
22. García-Segura, G.; Ricker, P.M.; Taam, R.E. Common Envelope Shaping of Planetary Nebulae. *ApJ* **2018**, *860*, 19, [arXiv:astro-ph.SR/1804.09309]. doi:10.3847/1538-4357/aac08c.
23. Zou, Y.; Frank, A.; Chen, Z.; Reichardt, T.; De Marco, O.; Blackman, E.G.; Nordhaus, J.; Balick, B.; Carroll-Nellenback, J.; Chamandy, L.; et al. Bipolar planetary nebulae from outflow collimation by common envelope evolution. *MNRAS* **2020**, *497*, 2855–2869, [arXiv:astro-ph.SR/1912.01647]. doi:10.1093/mnras/staa2145.
24. Dopita, M.; Hart, J.; McGregor, P.; Oates, P.; Bloxham, G.; Jones, D. The Wide Field Spectrograph (WiFeS). *Ap&SS* **2007**, *310*, 255–268, [0705.0287]. doi:10.1007/s10509-007-9510-z.
25. Dopita, M.; Rhee, J.; Farage, C.; McGregor, P.; Bloxham, G.; Green, A.; Roberts, B.; Neilson, J.; Wilson, G.; Young, P.; et al. The Wide Field Spectrograph (WiFeS): performance and data reduction. *Ap&SS* **2010**, *327*, 245–257, [arXiv:astro-ph.IM/1002.4472]. doi:10.1007/s10509-010-0335-9.
26. Danehkar, A. Discovery of Collimated Bipolar Outflows in the Planetary Nebula TH 2-A. *ApJ* **2015**, *815*, 35, [arXiv:astro-ph.SR/1512.02330]. doi:10.1088/0004-637X/815/1/35.
27. Danehkar, A.; Parker, Q.A. Spatially resolved kinematic observations of the planetary nebulae Hen 3-1333 and Hen 2-113. *MNRAS* **2015**, *449*, L56–L59, [arXiv:astro-ph.SR/1503.01551]. doi:10.1093/mnras/slv022.
28. Danehkar, A.; Parker, Q.A.; Steffen, W. Fast, Low-ionization Emission Regions of the Planetary Nebula M2-42. *AJ* **2016**, *151*, 38, [arXiv:astro-ph.SR/1601.01702]. doi:10.3847/0004-6256/151/2/38.
29. Danehkar, A. Morpho-kinematic properties of Wolf-Rayet planetary nebulae. *ApJS* **2022**, *accepted*, [arXiv:astro-ph.SR/2107.03994].
30. Danehkar, A. 3D spatio-kinematic modelling of Abell 48, a planetary nebula around a Wolf-Rayet [WN] star. *MNRAS* **2022**, *511*, 1022–1028, [arXiv:astro-ph.SR/2112.12043]. doi:10.1093/mnras/stab3735.
31. Ali, A.; Dopita, M.A.; Basurah, H.M.; Amer, M.A.; Alsulami, R.; Alruhaili, A. IFU spectroscopy of southern planetary nebulae - III. *MNRAS* **2016**, *462*, 1393–1404, [arXiv:astro-ph.SR/1607.00495]. doi:10.1093/mnras/stw1744.
32. Ali, A.; Dopita, M.A. IFU Spectroscopy of Southern Planetary Nebulae V: Low-Ionisation Structures. *PASA* **2017**, *34*, e036, [arXiv:astro-ph.SR/1707.09650]. doi:10.1017/pasa.2017.30.
33. Walsh, J.R.; Monreal-Ibero, A.; Barlow, M.J.; Ueta, T.; Wesson, R.; Zijlstra, A.A.; Kimeswenger, S.; Leal-Ferreira, M.L.; Otsuka, M. An imaging spectroscopic survey of the planetary nebula NGC 7009 with MUSE. *A&A* **2018**, *620*, A169, [arXiv:astro-ph.GA/1810.03984]. doi:10.1051/0004-6361/201833445.
34. Akas, S.; Monteiro, H.; Aleman, I.; Farias, M.A.F.; May, D.; Pereira, C.B. Exploring the differences of integrated and spatially resolved analysis using integral field unit data: the case of Abell 14. *MNRAS* **2020**, *493*, 2238–2252, [arXiv:astro-ph.GA/2002.12380]. doi:10.1093/mnras/staa383.
35. Monreal-Ibero, A.; Walsh, J.R. The MUSE view of the planetary nebula NGC 3132. *A&A* **2020**, *634*, A47, [arXiv:astro-ph.SR/1912.02847]. doi:10.1051/0004-6361/201936845.
36. García-Rojas, J.; Morisset, C.; Jones, D.; Wesson, R.; Boffin, H.M.J.; Monteiro, H.; Corradi, R.L.M.; Rodríguez-Gil, P. MUSE spectroscopy of planetary nebulae with high abundance discrepancies. *MNRAS* **2022**, *510*, 5444–5463, [arXiv:astro-ph.SR/2112.00480]. doi:10.1093/mnras/stab3523.
37. Acker, A.; Neiner, C. Quantitative classification of WR nuclei of planetary nebulae. *A&A* **2003**, *403*, 659–673. doi:10.1051/0004-6361:200303030.
38. Danehkar, A. Evolution of Planetary Nebulae with WR-type Central Stars. PhD thesis, Macquarie University, 2014. doi:10.5281/zenodo.47794.
39. Danehkar, A. Physical and Chemical Properties of Wolf-Rayet Planetary Nebulae. *ApJS* **2021**, *257*, 58, [arXiv:astro-ph.SR/2106.10762]. doi:10.3847/1538-4365/ac2310.
40. Crowther, P.A.; De Marco, O.; Barlow, M.J. Quantitative classification of WC and WO stars. *MNRAS* **1998**, *296*, 367–378. doi:10.1046/j.1365-8711.1998.01360.x.
41. Tylenda, R.; Acker, A.; Stenholm, B. Wolf-Rayet Nuclei of Planetary Nebulae - Observations and Classification. *A&AS* **1993**, *102*, 595.
42. Depew, K.; Parker, Q.A.; Miszalski, B.; De Marco, O.; Frew, D.J.; Acker, A.; Kovacevic, A.V.; Sharp, R.G. Newly discovered Wolf-Rayet and weak emission-line central stars of planetary nebulae. *MNRAS* **2011**, *414*, 2812–2827, [arXiv:astro-ph.SR/1101.2468]. doi:10.1111/j.1365-2966.2011.18337.x.
43. Basurah, H.M.; Ali, A.; Dopita, M.A.; Alsulami, R.; Amer, M.A.; Alruhaili, A. Problems for the WELS classification of planetary nebula central stars: self-consistent nebular modelling of four candidates. *MNRAS* **2016**, *458*, 2694–2709, [arXiv:astro-ph.SR/1602.08708]. doi:10.1093/mnras/stw468.

44. Wang, W.; Liu, X.W. Elemental abundances of Galactic bulge planetary nebulae from optical recombination lines. *MNRAS* **2007**, *381*, 669–701, [[0707.0542](#)]. doi:10.1111/j.1365-2966.2007.12198.x.
45. Stanghellini, L.; Shaw, R.A.; Villaver, E. The Magellanic Cloud Calibration of the Galactic Planetary Nebula Distance Scale. *ApJ* **2008**, *689*, 194–202, [[0807.1129](#)]. doi:10.1086/592395.
46. Frew, D.J.; Parker, Q.A.; Bojčić, I.S. The H α surface brightness-radius relation: a robust statistical distance indicator for planetary nebulae. *MNRAS* **2016**, *455*, 1459–1488, [[arXiv:astro-ph.SR/1504.01534](#)]. doi:10.1093/mnras/stv1516.
47. Akas, S.; López, J.A. Three-dimensional modelling of the collimated bipolar outflows of compact planetary nebulae with Wolf-Rayet-type central stars. *MNRAS* **2012**, *425*, 2197–2202, [[arXiv:astro-ph.SR/1206.5222](#)]. doi:10.1111/j.1365-2966.2012.21578.x.
48. Parker, Q.A.; Philipps, S.; Pierce, M.; et al.. The AAO/UKST SuperCOSMOS H α survey. *MNRAS* **2005**, *362*, 689–710, [[arXiv:astro-ph/0506599](#)]. doi:10.1111/j.1365-2966.2005.09350.x.
49. Derlopa, S.; Akas, S.; Boumis, P.; Steffen, W. High-velocity string of knots in the outburst of the planetary nebula Hb4. *MNRAS* **2019**, *484*, 3746–3754, [[arXiv:astro-ph.SR/1901.05767](#)]. doi:10.1093/mnras/stz193.
50. De Marco, O.; Crowther, P.A. The WC10 central stars CPD-56 deg8032 and He2-113 - II. Model analysis and comparison with nebular properties. *MNRAS* **1998**, *296*, 419–429. doi:10.1046/j.1365-8711.1998.01379.x.
51. Cohen, M.; Barlow, M.J.; Sylvester, R.J.; Liu, X.W.; Cox, P.; Lim, T.; Schmitt, B.; Speck, A.K. Water Ice, Silicate, and Polycyclic Aromatic Hydrocarbon Emission Features in the Infrared Space Observatory Spectrum of the Carbon-rich Planetary Nebula CPD -56 deg8032. *ApJ* **1999**, *513*, L135–L138. doi:10.1086/311914.
52. Cohen, M.; Barlow, M.J.; Liu, X.W.; Jones, A.F. The dual dust chemistries of planetary nebulae with [WCL] central stars. *MNRAS* **2002**, *332*, 879–890. doi:10.1046/j.1365-8711.2002.05350.x.
53. Chesneau, O.; Collioud, A.; De Marco, O.; Wolf, S.; Lagadec, E.; Zijlstra, A.A.; Rothkopf, A.; Acker, A.; Clayton, G.C.; Lopez, B. A close look into the carbon disk at the core of the planetary nebula CPD-56°8032. *A&A* **2006**, *455*, 1009–1018, [[arXiv:astro-ph/0606745](#)]. doi:10.1051/0004-6361:20054585.
54. Lagadec, E.; Chesneau, O.; Matsuura, M.; De Marco, O.; de Freitas Pacheco, J.A.; Zijlstra, A.A.; Acker, A.; Clayton, G.C.; Lopez, B. New insights on the complex planetary nebula Hen 2-113. *A&A* **2006**, *448*, 203–212, [[arXiv:astro-ph/0509014](#)]. doi:10.1051/0004-6361:20053803.
55. De Marco, O.; Barlow, M.J.; Storey, P.J. The WC10 central stars CPD-56 deg 8032 and He 2-113. I - Distances and nebular parameters. *MNRAS* **1997**, *292*, 86.
56. Lee, H.W.; Hyung, S. Broad H α Wing Formation in the Planetary Nebula IC 4997. *ApJ* **2000**, *530*, L49–L52, [[arXiv:astro-ph/astro-ph/99114](#)]. doi:10.1086/312479.
57. Steffen, W.; López, J.A. Morpho-Kinematic Modeling of Gaseous Nebulae with SHAPE. *Rev. Mex. Astron. Astrofis.* **2006**, *42*, 99–105, [[arXiv:astro-ph/0601585](#)].
58. Steffen, W.; Koning, N.; Wenger, S.; Morisset, C.; Magnor, M. Shape: A 3D Modeling Tool for Astrophysics. *IEEE Trans. Vis. Comput. Graphics* **2011**, *17*, 454–465. doi:10.1109/TVCG.2010.62.